



Oxidative reforming of model biogas over NiO–Y₂O₃–ZrO₂ catalysts

Yvan J.O. Asencios ^a, Cristiane B. Rodella ^b, Elisabete M. Assaf ^{a,*}

^a Instituto de Química de São Carlos, Universidade de São Paulo, Av. Trabalhador Sãocarlense, 400, 13560-970 São Carlos, SP, Brazil

^b Laboratório Nacional de Luz Síncrotron, Rua Giuseppe Máximo Solfaro, 10.000 Pólo II de Alta Tecnologia, 13083-970 Campinas, SP, Brazil

ARTICLE INFO

Article history:

Received 22 June 2012

Received in revised form 14 October 2012

Accepted 23 October 2012

Available online 24 November 2012

Keywords:

NiO–Y₂O₃–ZrO₂ catalysts

Polymerization method

Reforming reaction

Model biogas

Synthesis gas

ABSTRACT

Catalysts composed of NiO/Y₂O₃/ZrO₂ mixtures were synthesized by the polymerization method in a single step. They were characterized by X-ray diffraction (XRD), temperature-programmed reduction (TPR), physisorption of N₂ (BET) and X-ray photoelectron spectroscopy (XPS) and then tested in the oxidative reforming of a model biogas (1.5CH₄:1CO₂) in the presence of oxygen (1.5CH₄ + 1CO₂ + 0.25O₂) at 750 °C for 6 h. It was observed that the catalysts Ni20YZ and Ni40YZ performed better in catalytic processes than NiO/ZrO₂ and NiO/Y₂O₃, synthesized under the same conditions. The formation of Y₂O₃–ZrO₂ and NiO–Y₂O₃ solid solutions increased the rates of conversion of the reactants (CH₄ and CO₂) into synthesis gas (H₂ + CO). The formation of oxygen vacancies (in samples containing ZrO₂ and Y₂O₃) seemed to promote removal of the coke deposited on the nickel surface during the oxidative reforming of model biogas. The H₂/CO ratios in the reaction products formed on the best catalysts were 1:1, which is desirable for their direct use in the STD and in the Fischer–Tropsch processes.

© 2013 Published by Elsevier B.V.

1. Introduction

In the absence of oxygen, anaerobic bacteria break down the organic matter of biomass, producing a mixture of methane and carbon dioxide [1]. Raw biogas has an average composition of 55–65% CH₄, 30–45% CO₂, 0.5–2% H₂S and traces of H₂ and NH₃ [2–4]. This composition can vary with the origin of the biomass feedstock and the operational conditions. The anaerobic digestion of biomass is an attractive alternative way to produce biofuels and biofertilizer, given the increasing cost of energy.

Biogas is considered a first generation biofuel and its direct uses include electricity generation by internal combustion engine, or by cogeneration; it can also be used in vehicles, after slight adaptations [1]. However, the direct use of biogas has two main drawbacks due to the relatively high content of CO₂, which both lowers the heating value of biogas and contributes to greater emissions of CO₂ into the atmosphere [5].

Synthesis gas (syngas: H₂/CO) is a highly valued raw material for the petrochemical industry, and its production has an important role in the large-scale gas-to-liquid process [3]. Syngas is used in the synthesis of methanol and dimethyl ether (DME) and in the coupled syngas-to-dimethyl-ether process (STD) [6,7].

On the other hand, there are growing incentives to reduce greenhouse gas emissions, following the Kyoto Accord in effect in most of the world [8]. As the main constituents of biogas are CH₄ and

CO₂ (the two main greenhouse gases), the conversion of biogas into syngas is a very attractive strategy to reduce the emission of greenhouse gases. Thus, the production of syngas from biogas, which can be considered a renewable source material, can result in both economic and environmental advantages. For these reasons, biogas reforming has received much attention from researchers in recent years [4,9–12].

The average composition of the principal components of biogas, namely methane and carbon dioxide in a ratio of 1.5:1, is favorable to the dry reforming of methane (DRM, reaction (1)), as the required mixture of methane and carbon dioxide is present in the composition of biogas and no facilities for separation are needed:



It is well known that, during the DRM reaction, the reverse water-gas shift reaction (RWGSR, reaction (2)) can also be favored. Reaction (1) favors the production of syngas, with H₂/CO = 1, but a heavy coke deposit can be expected due to the excess of methane in the inlet stream. In this context, the addition of oxygen at the inlet may help to decrease the carbon deposit and increase the conversion of methane [4], as it can react with the excess methane in the inlet stream, in the partial oxidation of methane (POM):

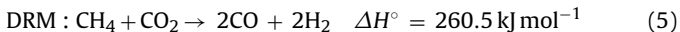


Several studies [13,14] have shown that in most cases, the POM reaction follows the combustion-reforming mechanism, in which the total combustion of methane (TCM) produces CO₂ and H₂O as

* Corresponding author. Tel.: +55 1633739951; fax: +55 1633739952.

E-mail address: assaf@iqsc.usp.br (E.M. Assaf).

primary products, and is followed by dry reforming of methane (DRM) and steam reforming of methane (SRM), to produce syngas:



The global sum of reactions (4)+(5)+2×(6) is reaction (3), with a H₂/CO ratio of 2. Thus, the addition of oxygen to the biogas results in the oxidative reform of methane and, according to the stoichiometry of the coupled process (reactions (1) and (3)), the resultant H₂/CO ratio is 1.2:1 (also called H₂-poor syngas). This H₂/CO ratio is desirable for the Fischer–Tropsch synthesis, for the production of formaldehyde and for the STD process [7,15].

Nickel-based catalysts have shown good activity in reforming reactions, comparable to that of catalysts based on noble metals (Pt, Ir, Rh, Pd and Ru), which are very expensive and of low availability [16]. However, Ni-based catalysts suffer from deposition of carbon during the reaction, which leads to deactivation. For this reason, much research has been focused on the improvement of nickel catalysts, to achieve enhanced activity and reduced coke deposits [17,18].

In recent years, ZrO₂ has been tested in methane-reforming reactions, because its high ionic conductivity and thermal stability are very useful for these reactions. The tetragonal phase of ZrO₂ is stabilized by adding cations, such as Mg⁺², Ca⁺², Sr⁺², La⁺³, Zn⁺², Ce⁺⁴ and Y⁺³, that form solid solutions resulting in oxygen vacancies in the zirconia lattice [19]. These oxygen vacancies have a very important role in gasifying carbon deposits and in the activation of CO₂ and O₂ molecules, as has been demonstrated in previous reports [20–25] on the methane reforming and ethanol reforming reactions.

In our previous report [18], it was found that Ni/Y₂O₃–ZrO₂ catalysts were active in the dry reforming of methane (maximum activity was reached at 8 mol% of Y₂O₃), but produced low H₂/CO ratios, owing to the considerable activity of the RWGSR. Moreover, it was not clear whether the solid solutions of NiO–Y₂O₃ and Y₂O₃–ZrO₂ made any specific contribution to catalysis of the reforming reaction or affected coke deposition, the latter being very important for scale-up studies. In the present study, we focus on the effect of relatively high loadings of additive (Y₂O₃) and of nickel in the NiO/Y₂O₃/ZrO₂ system, aiming to form the corresponding solid solutions; their effects on the catalytic reforming of model biogas (with or without the presence of oxygen) and on the type of coke deposited on the catalytic surface are discussed.

2. Experimental

2.1. Preparation of catalysts

The catalysts were prepared by the polymerization (Pechini) method in a single step, from mixtures of solutions of Ni(NO₃)₂·6H₂O (Aldrich); Zr(CO₃)₂·1.5H₂O (Aldrich) and Y(NO₃)₃·6H₂O (Aldrich), as described in a previous report [9]. The mole fraction of Y₂O₃ varied as follows: 0, 4, 20, 40 and 100%, relative to ZrO₂. Every catalyst had 20 wt% nickel. The three precursors were dissolved (the carbonate in nitric acid, the nitrates in water) and then mixed together into a solution of citric acid and ethylene glycol, and the polymeric precursor was formed by taking this mixture to 120 °C and keeping it at this temperature for 24 h. The products were heated at 10 °C min⁻¹ and calcined at 500 °C for 3 h and subsequently at 750 °C for 2 h, in synthetic air. Catalysts were designated NiZ, Ni4YZ, Ni20YZ, Ni40YZ and NiY, according to the molar percentage of Y₂O₃ in the mixture. For instance, in Ni4YZ, the mixture of NiO/Y₂O₃/ZrO₂ had 4 mol% Y₂O₃ relative to

ZrO₂; in NiZ and NiY, only two oxides were mixed, nickel oxide with pure zirconia or yttria. For the purpose of comparison, a sample containing 20 wt% Ni (same concentration as in the NiYZ catalysts) supported on a commercial alumina (220 m² g⁻¹) was synthesized (sample NiAlcom) and then heat-treated under the same conditions as the other catalysts.

2.2. Characterization

The crystal phases were identified with a Rigaku Multiflex X-ray diffractometer (30 kV–10 mA) by recording patterns in the range 2θ=5–80°, at a scan speed of 2° min⁻¹, using Cu Kα radiation (λ = 1.5406 Å). An *in situ* X-ray diffraction study was carried out with a 6-circle diffractometer (Huber) at the beamline D10B-XPD of the Brazilian Synchrotron Light Laboratory (LNLS) in Campinas, Brazil. The X-ray wavelength used was 1.5406 Å and the Bragg angle was scanned continuously in the range 2θ=25–70° at an angular speed of 0.02° s⁻¹. Approximately 100 mg of the powder sample was placed in a ceramic sample holder. The XRD pattern was acquired under reduction conditions, for which purpose the catalyst was heated in a 50 mL min⁻¹ H₂ stream (5% H₂/He) from room temperature to 800 °C, at a rate of 5 °C min⁻¹. The XRD pattern was collected *in situ* at 800 °C for each catalyst.

The specific surface area (BET) was estimated from the N₂ adsorption/desorption isotherms at liquid nitrogen temperature, using a Quantachrome Nova 1200 instrument. Temperature-programmed reduction (TPR) was performed in a quartz tube reactor and hydrogen consumption was measured in-line with a thermal conductivity detector (TCD). 100 mg of catalyst was placed in the TPR reactor and reduced with a 5% H₂–95% He (v/v) gas mixture flowing at 30 mL min⁻¹. The temperature was raised to 1000 °C at a heating rate of 5 °C min⁻¹. The amount of H₂ consumed was calibrated with a standard CuO powder.

Scanning electron microscopy (SEM) images of spent catalysts were taken in a LEO 440 microscope with an Oxford detector, operating with a 20 kV electron beam. The samples were made up in the form of pellets and coated with a layer of gold to avoid a build-up of charge.

The composition of the catalysts was determined by energy-dispersive X-ray spectroscopy (EDX), using a LEO 440 scanning electron microscope with a tungsten filament coupled to an energy-dispersive X-ray detector; measurements were made in five regions of the image.

Fresh catalysts were analyzed by X-ray photoelectron spectroscopy (XPS) with a PHOIBOS150 hemispherical spectrometer from SPECS (Berlin, Germany), using the HSA3500 high-volt power supply, in operation at the Brazilian Synchrotron Light Laboratory (LNLS) in Campinas, Brazil. The XPS had a monochromatic Al Kα (hv = 1486.6 eV) source and a nine-channel electron multiplier detector. The monochromatic source was operated at 10 kV and 10 mA and the spectra were recorded with analyzer pass energy of 20 eV. The samples in powder form were supported on copper double-sided tape fixed on the XPS sample holder. The spectra were analyzed with the program CasaXPS, version 2.2.99. The binding energies were referenced to the C 1s line at 284.5 eV, from the carbon on the tape. The deconvolutions for the Ni 2p, Zr 3d, Y 3d, O 1s and C 1s levels were obtained by curve fitting to Gaussian line-shapes, after subtracting the Shirley background function. Each peak was analyzed quantitatively by dividing the integrated area under the peak by the atomic sensitivity factor, taking the sensitivity factor of C 1s as 1.0 (binding energy of 284.5 eV).

2.3. Model biogas reforming reaction

Catalytic reactions were carried out with 100 mg of catalyst in a fixed-bed down-flow quartz reactor (i.d. = 10 mm) connected

downstream to a gas chromatograph fitted with a thermal conductivity detector. Prior to reactions, the catalysts were activated by reduction with H_2 (30 mL min^{-1}) at 800°C for 1 h. Next, the sample was brought to the reaction temperature (750°C) under a flow of pure N_2 . The reaction temperature was measured and controlled by a thermocouple inserted into the top of the catalyst bed.

The catalysts were tested under two conditions:

Dry reforming of methane of a model biogas: a molar feed ratio of $1.5\text{CH}_4:1\text{CO}_2$, was used to simulate a biogas with a typical ratio (60% of CH_4 and 40% of CO_2), flowing at 43.5 mL min^{-1} of CH_4 , 29 mL min^{-1} of CO_2 and 34.8 mL min^{-1} of N_2 , resulting in a total flow of 107.3 mL min^{-1} inside the reactor.

Oxidative reform of a model biogas (combination of dry reforming of methane and partial oxidation of methane): the feed was a mixture of the model biogas and oxygen (O_2 in synthetic air 21%) in a molar ratio of $1.5\text{CH}_4:1\text{CO}_2:0.25\text{O}_2$; 43.5 mL min^{-1} of CH_4 , 29 mL min^{-1} of CO_2 and 7.3 mL min^{-1} of O_2 (34.8 mL min^{-1} of synthetic air 79% N_2 and 21% O_2), giving a total flow of 107.3 mL min^{-1} inside the reactor.

All reactions were carried out at 750°C . The unconverted reactants and all the reaction products were analyzed in-line with a gas chromatograph (GC, Varian 3800) with an automatic injection valve. The products at the reactor outlet were divided into two streams which were analyzed differently, in order to obtain a complete analysis of the reaction products. In one stream, H_2 and CH_4 were separated on a 13X molecular sieve packed column, with nitrogen as carrier gas. In the other stream, helium was used as the carrier gas and CO_2 , CH_4 and CO were separated on 13X molecular sieve and Porapak-N packed columns. Both GC outlets were equipped with thermal conductivity detectors.

Carbon deposition was measured as the apparent gain in mass of the catalyst during the 6 h of reaction.

The CH_4 and CO_2 conversions were calculated as:

$$\text{Rconversion}(\%) = (\text{MolsRin} - \text{MolsRout}) / (\text{MolsRin}), \text{ where R is CH}_4 \text{ or CO}_2.$$

3. Results and discussion

3.1. Catalyst characterization

Fig. 1 shows X-ray diffraction (XRD) patterns of the catalysts and the lattice parameters for ZrO_2 and NiO are in **Table 1**. **Fig. 1a** shows that peaks for monoclinic ZrO_2 (JCPDS 83-0944) in NiZ disappeared on addition of Y_2O_3 (in samples Ni4YZ , Ni20YZ and Ni40YZ), indicating that the addition of Y^{+3} stabilizes the tetragonal ZrO_2 (JCPDS 81-1549) at room temperature, by forming a Y_2O_3 – ZrO_2 solid solution [18,26]. Thus, the Y^{+3} ion probably dissolves in the crystal lattice of ZrO_2 , replacing some Zr^{+4} ions at the lattice site and resulting in the generation of oxygen vacancies to compensate for the difference between the oxidation states of Y^{+3} and Zr^{+4} . This finding is supported by the observed expansion of the lattice parameter of ZrO_2 (**Table 1**), which suggests that Y^{+3} (ionic radius 0.93 Å) entered the ZrO_2 crystal lattice (ionic radius $\text{Zr}^{+4} = 0.84\text{ \AA}$), and by the continuous displacement of the principal peak (1 1 1) of the tetragonal ZrO_2 to lower Bragg angles (**Fig. 1c**) [27,28]. It is also noted that the peak attributed to tetragonal ZrO_2 (**Fig. 1c**) becomes broader with increasing Y_2O_3 content, indicating a diminution of the size of crystallites.

On the other hand, **Fig. 1b** shows that a peak related to NiO shifted to lower values of 2θ as the Y_2O_3 loading increased. This effect is due to the diffusion of Y^{+3} (ionic radius 0.93 Å) ions into the NiO crystal lattice ($\text{Ni}^{+2} = 0.78\text{ \AA}$) to form a NiO – Y_2O_3 solid solution [27,28], resulting in the enlargement of the lattice parameter of NiO (**Table 1**). This conformation is possible because NiO and Y_2O_3 both have face-centered cubic (fcc) structures and appropriate ionic sizes [28].

Table 1 Binding energies of main peaks, atomic fractions of Ni, Zr and Y determined by XPS analysis and lattice parameters obtained by XRD analysis.

Sample	Binding energy (eV)			%Atomic percent on the surface (XPS)			% Atomic percent in the bulk (theoretical values)			Lattice parameter (Å)				
	$\text{Ni } 2\text{p}_{3/2}$	$\text{Zr } 3\text{d}_{5/2}$	$\text{Y } 3\text{d}_{5/2}$	$Zn/(Zr + Ni + Y)$	$Ni/(Zr + Ni + Y)$	$Y/(Zr + Ni + Y)$	Zr	Ni	Y	$a(\text{ZrO}_2)$	$a(\text{NiO})$			
NiY	854.9	—	155.9	—	6.1	93.9	—	32.48	67.52	—	33.68	66.32	—	4.18
Ni40YZ	854.6	181.6	156.4	53.4	21.5	25.1	36.91	33.57	29.52	36.14	34.50	29.36	5.26	4.18
Ni20YZ	854.8	181.8	156.8	64.4	19.8	15.8	47.23	33.88	18.89	44.93	33.29	21.78	5.16	4.18
Ni4YZ	854.8	181.8	157.8	88.3	9.10	2.5	60.85	34.28	4.87	57.82	36.85	5.33	5.11	4.17
NiZ ^a	855.0	182	—	85.8	14.2	—	65.58	34.42	—	60.30	39.70	—	5.09	4.16

^a Data reported in a previous work [16].

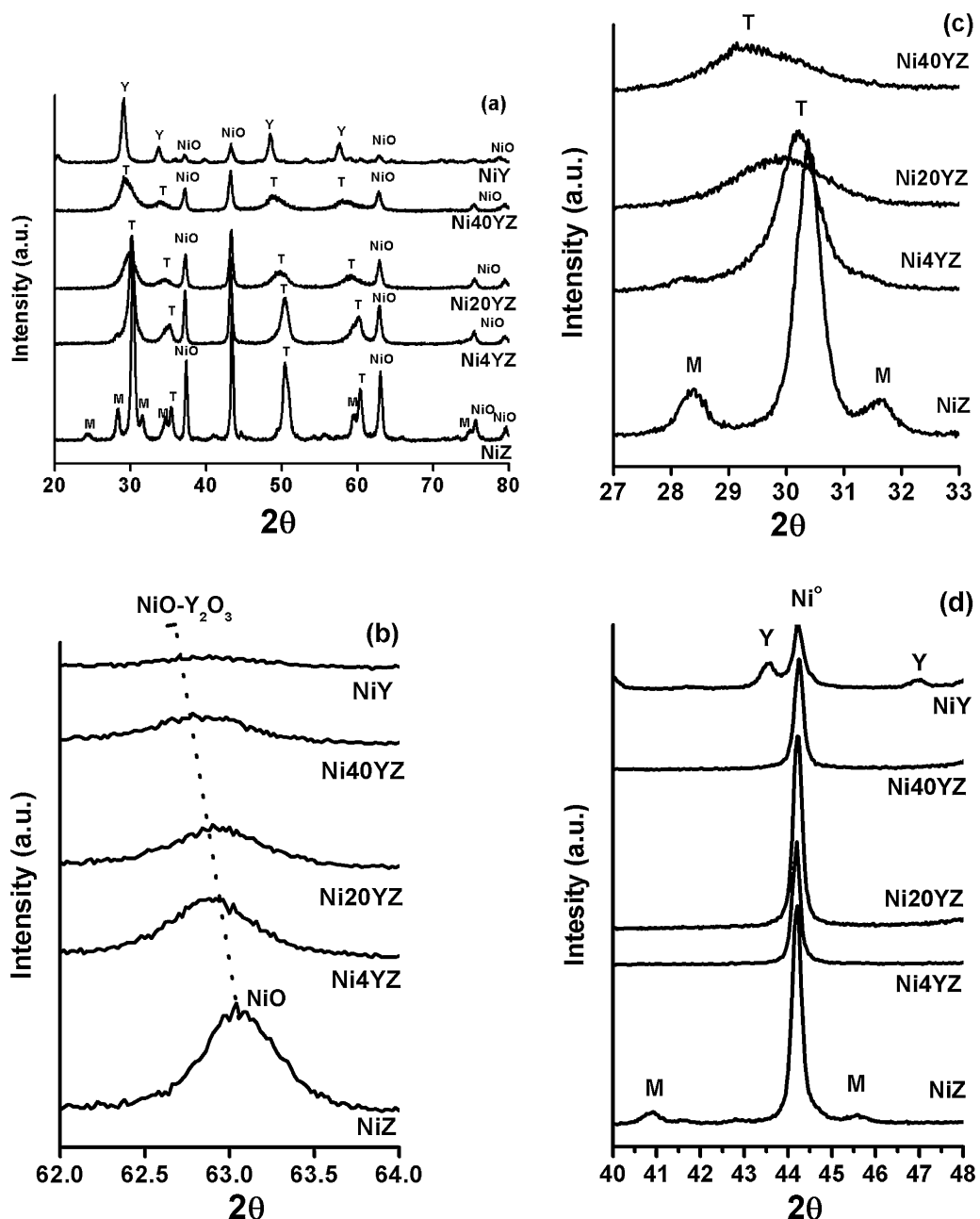


Fig. 1. XRD patterns of oxides of synthesized catalysts: (a) aligned XRD patterns of the oxides, (b) enlargement of pattern between Bragg angles 62° and 64°, (c) enlargement of pattern between Bragg angles 27 and 33°, (d) enlargement of pattern collected *in situ* between angles 40° and 48° of the H₂-reduced catalysts at 800 °C (T: tetragonal phase of ZrO₂, M: monoclinic phase of ZrO₂).

The results obtained by *in situ* XRD of the catalysts under reduction with H₂ at 800 °C, are shown in Fig. 1d. In this figure, the principal peak of Ni° of each pattern of catalysts is shown, the crystallite size (d , nm) were calculated by the Scherrer equation [29], these values are shown in Table 3.

To estimate the metal dispersion (D_M) of the active phase of the catalysts, some authors [29–32] employed the following equation, valid for a population of spheroidal particles of the metal phase: $D_M = 101/(d)$, where (d) is the average crystallite size of Ni°, expressed in nm, and the constant is calculated on the basis of an assumed spherical particle and the density of nickel atoms on a polycrystalline Ni surface (1.54×10^{19} atom Ni m⁻²).

Several authors [29,33–38], have shown that the values for metal dispersion obtained by chemisorption techniques (chemisorption of H₂ or CO) agree well with the XRD estimates.

In the XRD estimates, d was calculated by the Scherrer equation [29] from XRD pattern of reduced catalysts. The estimates values for D_M are given in Table 3. According to these values, Ni4YZ and NiY catalysts reached the highest metal dispersion, suggesting that the addition of Y₂O₃ produced no definite trend in the dispersion of Ni°. This fact has a direct influence on the catalytic performance of the synthesized material, as will be explained in the catalytic test section.

Photoelectron spectroscopy (XPS) was used to obtain further information about the valency/oxidation state of the elements on the surface and the surface composition of the NiO–Y₂O₃–ZrO₂ catalysts. It is important to remember that the binding energy (BE) of the core levels, revealed by XPS, is influenced by the chemical bonds and by the local environment of the atom on the surface. This is relevant to the case of ZrO₂ in the presence of Y₂O₃ and NiO.

Table 2

Integrated areas of TPR peaks of the supports.

Supports	H_2 consumed ($\text{mol H}_2 \times 10^{-5}$ ^a)			Surface area ($\text{m}^2 \text{ g}^{-1}$)
	ρ	θ	Total	
ZrO ₂	1.67	—	1.67	19
Y ₂ O ₃	—	—	0.67	23
4YZ	1.57	0.27	1.84	40
20YZ	1.39	4.94	6.33	35
40YZ	0.97	10.9	11.8	15

^a Experimental value for 80 mg of sample. ρ , θ are the reduction peaks of each support; for more details see the text.

On raising the Y₂O₃ content from 4 to 40 mol%, the increasing number of structural oxygen vacancies formed in the Y₂O₃–ZrO₂ lattice change the number of oxygen sites around Zr atoms [39]. Thus, the change in coordination number of Zr atoms (from the monoclinic to tetragonal crystal lattice) is confirmed by the change in the measured binding energies (BE) of Zr 3d_{5/2} core levels (Table 1) [40].

The BE of 182 eV for Zr 3d_{5/2} in NiZ indicates that this zirconium was in the form of ZrO₂ and that the addition of NiO to ZrO₂ did not modify the environment of Zr⁴⁺ [40]. This BE decreased slightly in samples Ni4YZ, Ni20YZ and Ni40YZ, showing that some electron transfer from Y³⁺ to Zr⁴⁺ took place, increasing the interaction between these cations and thus leading to the formation of a solid solution, as suggested previously by the XRD analysis. The BE values for Y 3d_{5/2} in samples Ni4YZ, Ni20YZ and Ni40YZ, which are slightly above the theoretical value for Y³⁺ (156 eV [41]), indicate the presence of yttrium in the form of Y³⁺ in the Y₂O₃–ZrO₂ solid solution, in which electron transfer has taken place from Y³⁺ to Zr⁴⁺. Parmigiani et al. [39] studied the Y₂O₃–ZrO₂ solid solution and found that when the content of Y₂O₃ is between 12 and 24 mol%, the binding energy of the zirconium core level (181.8 eV) is independent of the amount of Y₂O₃ in the mixture. In the present report, however, it is seen (Table 1) that this value is affected by larger amounts of Y₂O₃ in the mixture, as in the sample with 40 mol% (Ni40YZ).

The high intensity peak at 155.9 eV and the noticeable shoulder at 156.4 eV in the XPS profile of sample NiY (Table 1), which only contained NiO and Y₂O₃, indicate the presence of yttrium in two different environments, probably corresponding to Y³⁺ in Y₂O₃ and Y³⁺ in the NiO–Y₂O₃ solid solution. The presence of these lattice oxides was noted previously in the XRD analysis.

The theoretical value of BE for Ni 2p_{3/2} in Ni²⁺ (in NiO) is 855 eV [21]. The observed BE for Ni in sample NiZ was very close to this value, implying that there were only weak interactions between NiO and ZrO₂. The slight decrease in BE for Ni in NiY, Ni4YZ, Ni20YZ and Ni40YZ can be interpreted in terms of electron transfer from Y³⁺ to Ni²⁺, implying the formation of a NiO–Y₂O₃ solid solution, as suggested previously by the XRD analysis.

The relative atomic concentrations of Ni, Y and Zr on the surface of the catalysts were calculated from the peak areas of Ni 2p_{2/3}, Y 3d_{5/2} and Zr 3d_{5/2}, as described in the methods, and these results are shown in Table 1. As expected, the surface of NiO–Y₂O₃–ZrO₂ catalysts was enriched in yttrium and impoverished in zirconium as the Y₂O₃ loading increased in Ni4YZ, Ni20YZ and Ni40YZ.

From the Ni concentration on the surface, it is clear that as the Y₂O₃ increased to 20 mol% and 40 mol%, the quantity of nickel atoms on the surface increased progressively, showing that at higher Y₂O₃ loadings the migration of nickel atoms to the surface was favored. Finally, there was only a small amount of nickel on the surface of sample NiY, compared to that on the surface of the other samples, owing probably to the strong interaction between NiO and Y₂O₃, which form a NiO–Y₂O₃ solid solution, thus favoring the internal diffusion of nickel atoms into the bulk. The atomic concentrations of nickel on the catalytic surface are consistent with the

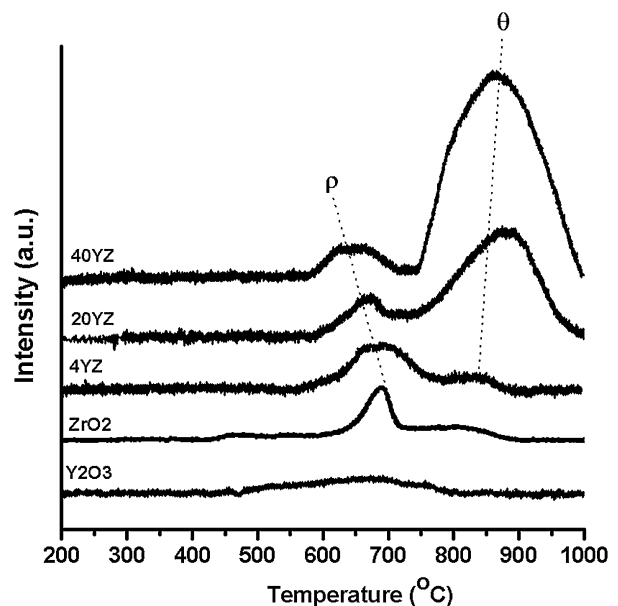


Fig. 2. TPR profiles of supports and precursor oxides.

dispersion of the metallic phase estimated by XRD (see Table 3), as the highest values of D_M correspond to NiY and Ni4YZ, which have the lowest atomic % Ni on surface.

It is known that a solid solution containing NiO can favor a finely dispersed active phase of Ni as a result of the diffusion of Ni into the bulk of the support. As shown by Parmaliana et al. [42], Hu and Ruckenstein [43] and by Ruckenstein and Wang [44], a quasi-uniform distribution of small Ni particles arises from the reduction of Ni²⁺ ions dispersed in a NiO–MgO solid solution, and of Co particles from Co²⁺ ions dispersed in a CoO–MgO solid solution. Moreover, in our previous reports (Asencios et al. [9,16]) we observed similar behavior for mixtures based on NiO–MgO in the presence of ZrO₂.

In the present study, a similar result was found only for sample NiY (which only contained NiO/Y₂O₃), on which the D_M was the highest and the atomic % of Ni on the surface was the lowest recorded (see Tables 1 and 3).

Conversely, in the three-oxide mixture, NiO/Y₂O₃/ZrO₂, the more NiO–Y₂O₃ solid solution was formed, the more nickel was found on the catalyst surface (see atomic % of Ni on the surface, Table 1). Thus, the idea that NiO–Y₂O₃ solid solution favors the diffusion of Ni into the bulk of the support and that, consequently, it favors the finer dispersion of Ni on the surface is not valid for the mixture of three oxides NiO–Y₂O₃–ZrO₂.

The chemical composition of the fresh catalysts was measured by EDX in five regions of the SEM image, and the average values are shown in Table 1. The measured contents of Ni, Zr and Y (atomic %) were very similar to the theoretical values (also shown in Table 1) for each component. Since the sampling depth of EDX is approximately 1 μm, the results were interpreted as approximate values for the bulk material [45]. Thus, Ni is less concentrated on the surface (see composition obtained by XPS), than in the bulk (see values obtained by EDX). The fall in atomic % of Ni at the surface (compared to bulk) is most noticeable in NiY, probably due to the diffusion of Ni²⁺ caused by the NiO–Y₂O₃ solid solution in this sample, as observed also for NiO/MgO solid solution [16].

The Y₂O₃–ZrO₂ (YZ) supports were analyzed by TPR to obtain further information about the role of the oxygen vacancies formed by Y₂O₃–ZrO₂ in the reduction of the catalytic NiO particles. Fig. 2 shows the TPR profiles of the YZ supports, ZrO₂ and Y₂O₃. All peaks were integrated to estimate their individual H₂ consumption and

Table 3

Integrated TPR peak areas of the catalysts expressed in moles of H₂; crystallite size (*d*, nm) and metal dispersion (DM).

Catalizador	H ₂ consumed (mol H ₂) × 10 ⁻⁴	% Reduction NiO	<i>d</i> (nm) (Ni ⁰)	DM
	α (NiO)	$\rho + \theta$		
NiZ ^a	3.19	—	36.8	2.8
Ni4YZ	2.60	1.09	23.4	4.3
Ni20YZ	2.28	1.20	33.6	3.0
Ni40YZ	2.21	1.32	30.9	3.3
NiY	2.91	0.18	21.8	4.6

^a Data reported in a previous work [21].

these results are shown in Table 2. The H₂ consumption of pure ZrO₂ and Y₂O₃ corresponded respectively to 2.56% and 1.88% of the total reduction of these oxides. Yttria is not easily reduced by hydrogen and shows a weak reduction peak up to 500 °C. Such a low level of reduction can be explained if the reduction of Y³⁺ to Y²⁺ occurred only on or near the surface of this oxide [46]. The peak ρ in the TPR profile for pure ZrO₂ is due to the consumption of H₂ by the surface-capping oxygen ions on the surface of zirconia. Analyzing the TPR profiles of the YZ supports, it is clear that the reduction of each oxide does not follow its own separate reduction profile when combined in the support, because the consumption of the support is higher than those of the separate oxides. According to the values for H₂ consumption in Table 2, higher Y₂O₃ loading in the support leads to the consumption of more H₂. This means that the oxygen vacancies generated in the Y₂O₃–ZrO₂ solid solution enhanced the reduction of the YZ supports.

Two peaks (ρ and θ) can be distinguished, in every YZ support profile. The H₂ consumption of peak ρ in 4YZ decreases as the content of Y₂O₃ is increased, while the H₂ consumption of peak θ increases steadily as the Y₂O₃ loading rises from 4 to 40% (Table 2).

As mentioned above, peak ρ is due to the reduction of the surface-capping oxygen ions of the YZ supports, located beside oxygen vacancies on the surface. This peak was also described by Dow and Huang [46] and by Bellido and Assaf [18] and those authors found similar values of H₂ consumption to those in the present report (1.57×10^{-5} mol H₂ per 80 mg sample) for a loading of 4 mol% Y₂O₃ in the YZ support. The continuous fall in the H₂ consumption related to peak ρ with rising yttria (see Table 2) is probably due to the drop in the surface area from $39.69 \text{ m}^2 \text{ g}^{-1}$ in 4YZ to $14.64 \text{ m}^2 \text{ g}^{-1}$ in 40YZ. In these YZ supports, it is possible that a support with a larger surface area exposes more surface oxygen vacancies and thus possesses more surface-capping oxygen ions to be reduced on the surface.

On the other hand, the consumption of H₂ related to peak θ increased steadily with Y₂O₃ loading, implying that a greater number of H₂ molecules were activated for the reduction. This peak is attributed to the introduction of Y³⁺ into the ZrO₂ lattice to form the solid solution, thus generating oxygen vacancies to compensate for the difference between the oxidation states of Zr⁴⁺ and Y³⁺, maintaining the electroneutrality of the lattice. In this light, the steady rise in the area of peak θ with rising Y₂O₃ loading implies the continuous formation of oxygen vacancies.

When Bellido and Assaf [18] studied the Y₂O₃–ZrO₂ system, they used a low loading of Y₂O₃ in the mixture, rising to a maximum of 12 mol%. In the TPR analysis they found the same peaks ρ and θ around 750 °C and 900 °C respectively, which are consistent with the peaks found in the present YZ supports. This is to be expected, since the same sample preparation method was employed. Additionally, those authors found a third peak (ω), very close to 950 °C, which was not found in the present study. This difference may be attributed to the larger amount of Y₂O₃ used in the present research, as the broader area of peak θ at larger Y₂O₃ loadings would be superimposed on a peak ω near 950 °C.

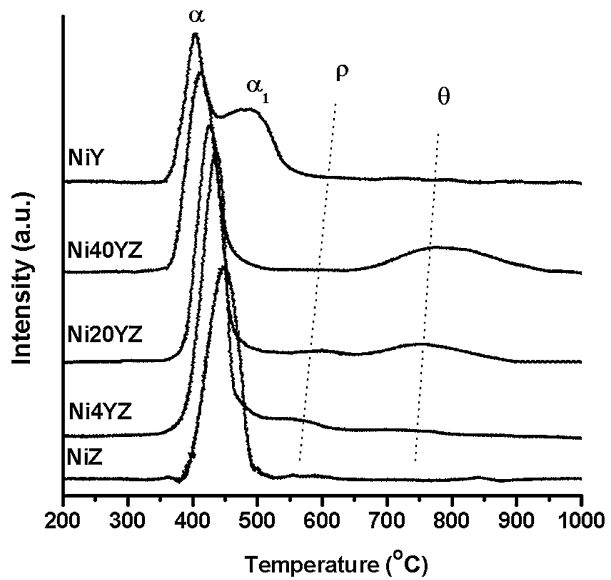


Fig. 3. Superposed TPR profiles of synthesized catalysts.

One interesting finding is the continuous displacement of peak ρ to lower temperatures at larger Y₂O₃ loadings. This implies that the higher loading of the additive modified the environment of the species responsible for peak ρ , so that the available surface-capping oxygens in the vicinity of oxygen vacancies were reduced more easily (since the reduction temperature fell).

Fig. 3 shows the TPR profiles of the synthesized catalysts. Two distinct regions can be seen: the first, located at low temperature (peak α), is associated with the reduction of NiO on the surface ($\text{NiO} + \text{H}_2 \rightarrow \text{Ni}^\circ + \text{H}_2\text{O}$) and the second, located at high temperature, is due to reduction of the catalytic supports (peaks ρ and θ). Peak areas in moles of hydrogen consumed are summarized in Table 3.

Sample NiY has two peaks for NiO reduction, α and α_1 , which overlap and can be associated with NiO species that interact weakly and strongly with the support surface (NiO species interacting strongly with the surface being reduced at the higher temperature). The presence of strongly interacting NiO species may be related to the ability of NiO and Y₂O₃ to form a solid solution, as noted in the XRD analysis, due to favorable conditions such as the similar crystal structures (fcc) and appropriate ionic sizes (0.78 Å and 0.93 Å for Ni²⁺ and Y³⁺ respectively). This solid solution may have implications for catalyst performance, as will be discussed later.

The continuous shift of peak α to lower temperature with rising Y₂O₃ loading may be due to the progressive formation of oxygen vacancies as Y₂O₃ is added to the mixture. These oxygen vacancies can facilitate the reduction of NiO, by interacting strongly with the boundary terminal oxygen ion of nickel oxide, weakening the Ni–O bond, and/or by polarizing H₂ molecules (H[−]···H⁺), which react with the oxygen of NiO clusters [9,16,46].

On the other hand, larger amounts of added Y₂O₃ decreased the % reduction of NiO, which reached a minimum of 64.92% on the sample containing 40 mol% Y₂O₃. Thus, the reduction of NiO on the catalysts may be hindered in the case of the strong interaction between NiO and Y₂O₃ (owing to the formation of the solid solution). However, if only this solid solution were involved in this process, the H₂ consumption of NiY would be close to or even lower than the H₂ consumption by samples containing the three oxides, but, as observed in Table 3, this value is higher (NiY(85.5%)>Ni4YZ(76.3%)>Ni20YZ(66.9%)>Ni40YZ(64.9%)), meaning that an additional effect inhibits the reduction of NiO in 3-oxide mixtures. This may be caused by the presence of Ni²⁺ ions dissolved in the tetragonal ZrO₂ crystal lattice, which

Table 4

Rates of carbon deposition (mmol Ch^{-1}) for the catalysts during the dry reforming and oxidative reforming of model biogas.

Sample	Dry-reforming mmol Ch^{-1}	Oxidative reform mmol Ch^{-1}
NiZ	0.10	0.07
Ni4YZ	0.76	0.15
Ni20YZ	0.96	0.14
Ni40YZ	0.84	0.42
NiY	1.10	0.10

suffered an expansion of the lattice parameter on formation of the $\text{Y}_2\text{O}_3\text{-ZrO}_2$ solid solution, allowing Ni^{+2} to enter the ZrO_2 crystal lattice. Similar results were found by Yin et al. [27]. Moreover, this fact may explain the disappearance of peak $\alpha 1$ in samples containing 3-oxide mixtures (NiO species interacting strongly with the support surface); probably these ions (Ni^{+2}) migrate to the bulk of the $\text{Y}_2\text{O}_3\text{-ZrO}_2$ solid solution, where they cannot be reduced to Ni° .

According to the value for NiO reduction in NiZ (93.62%) in Table 2, most of the NiO interacts weakly with ZrO_2 . This finding would confirm that no solid solution is formed between NiO and ZrO_2 , as was observed in the XRD analysis, where total stabilization of tetragonal ZrO_2 occurs only on the addition of Y_2O_3 .

3.2. Catalytic activity

Catalysis of the dry reforming of methane in a model biogas ($\text{CH}_4:\text{CO}_2 = 1.5:1$) was carried out on the synthesized samples and the results are shown in Fig. 4a–c. The catalytic tests show that the conversion rates of CH_4 decreased as follows: Ni4YZ > NiY > Ni20YZ > NiZ > Ni40YZ. Except for sample NiY, all the catalysts show stability during the reaction. This trend indicates that Ni4YZ and NiY had high activity for methane decomposition, suggesting that these samples have a good conformation of Ni° active sites to break the C–H bond of methane. This may be related to the fact that these two samples possess the highest Ni° dispersion and the lowest atomic % of Ni° on the surface (see Tables 1 and 3), suggesting that the lower concentration of nickel on the surface leads to a good conformation of active sites for the dry reforming of biogas. A similar finding was reported in our previous work [16] for mixtures of NiO–MgO– ZrO_2 .

NiY had a high catalytic activity but showed rapid deactivation due to the large amount of coke deposited. The contrary was observed for NiZ, Ni20YZ and Ni40YZ (low catalytic activity), which had the lowest nickel dispersion and the highest concentration of Ni° on the surface (Tables 1 and 3), probably due to a poor conformation of active sites for the dry reforming of biogas.

In all cases, the conversion of CH_4 was lower than the conversion of CO_2 , indicating the occurrence of the RWGSR ($\text{CO}_2 + \text{H}_2 \leftrightarrow \text{CO} + \text{H}_2\text{O}$), which was confirmed by the traces of water collected after each reaction. This finding can also explain why the H_2/CO ratio is lower than 1 (Fig. 4c). Under the reaction conditions studied, the catalytic supports (YZ) did not show any catalytic activity in the dry reforming of methane.

As explained in Section 1 of this report, the addition of oxygen in the dry reforming of biogas ($1.5\text{CH}_4:1\text{CO}_2$) could improve the CH_4 conversion, decrease the carbon deposition rates by gasifying carbon species (as demonstrated by Lucedio et al. [4]) and provide syngas with H_2/CO ratios suited to direct use in the Fischer–Tropsch process and/or in the STD process. The results for the reforming of the model biogas in the presence of oxygen (added in the form of air) are shown in Fig. 5a–c.

According to these results, the addition of oxygen increased the conversion of CH_4 and reduced the conversion of CO_2 on all catalysts. The conversion rates of CH_4 decreased as follows:

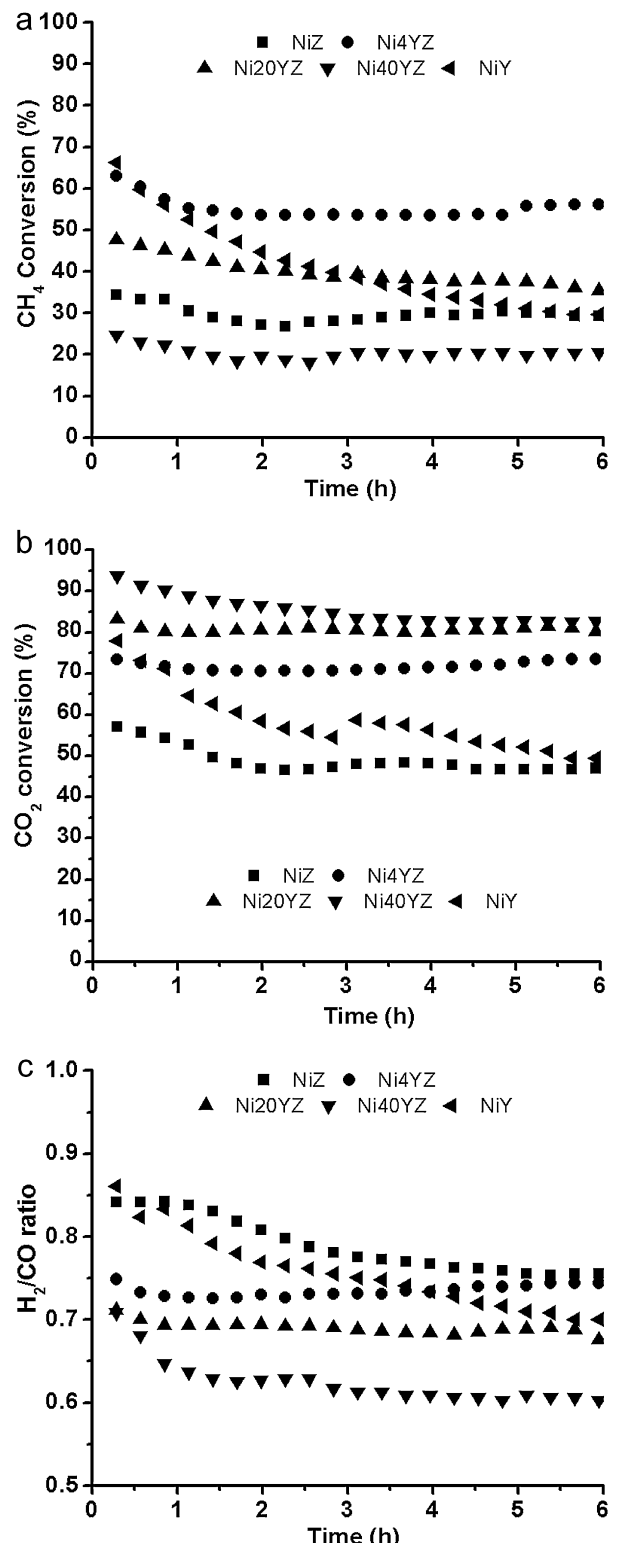


Fig. 4. Percent conversion of reactants in dry reforming of model biogas vs reaction time (h) (conditions: $T = 750^\circ\text{C}$, $\text{CH}_4:\text{CO}_2 = 1.5:1$): (a) CH_4 conversion, (b) CO_2 conversion and (c) H_2/CO ratio in the products.

$\text{Ni40YZ} > \text{Ni20YZ} > \text{Ni4YZ} > \text{NiY} > \text{NiZ}$. This order is very different from that found for the reaction without the addition of oxygen.

Now, in Fig. 5a it is seen that the conversion rate of CH_4 increased with Y_2O_3 content up to 40%. One of the factors that may be involved in this trend is the oxygen vacancies formed in the $\text{Y}_2\text{O}_3\text{-ZrO}_2$ solid solution, which can activate the O_2 molecules to react readily

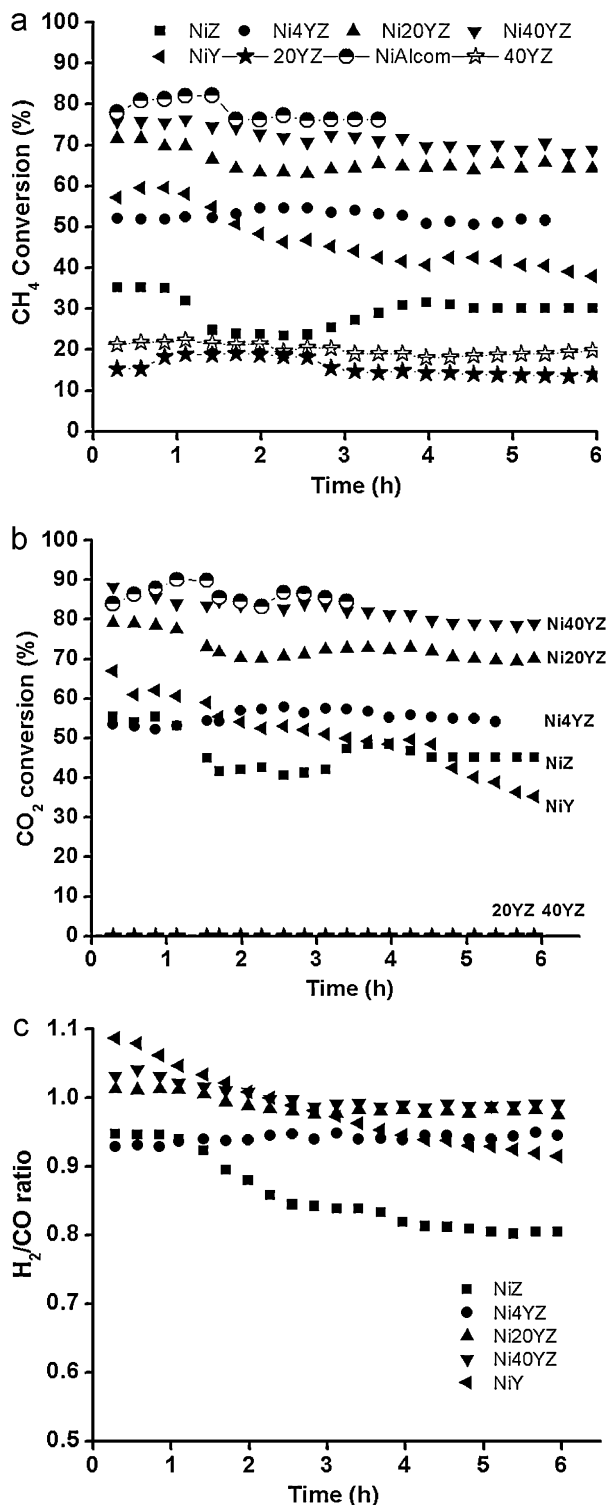


Fig. 5. Percent conversion of reactants in oxidative reforming of model biogas vs reaction time (h) (conditions: $T = 750^\circ\text{C}$, $\text{CH}_4/\text{CO}_2/\text{O}_2 = 1.5/1/0.25$): (a) CH_4 conversion, (b) CO_2 conversion and (c) H_2/CO ratio in the products.

with CH_4 molecules [47]. A high concentration of oxygen vacancies favors dissociation of oxygen molecules to form various oxygen species adsorbed on the surface: O_2^- , O_2^{2-} , O^{2-} , O^- [48,49].

By this reasoning, the presence of $\text{Y}_2\text{O}_3-\text{ZrO}_2$ solid solution may favor the POM reaction, so that catalysts with more solid solution in their composition are better for the POM reaction. This was confirmed by the fact that when oxygen was added to the inlet stream,

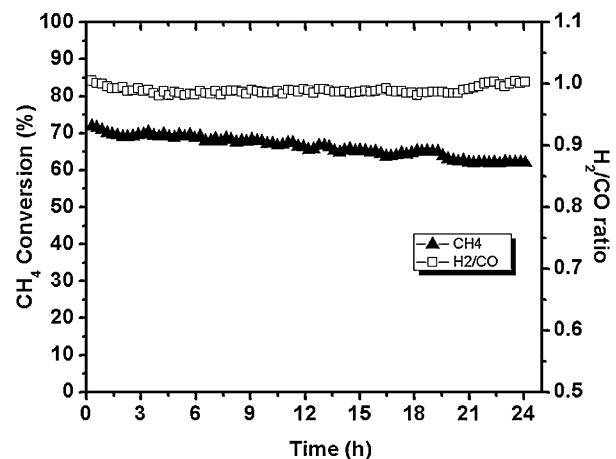


Fig. 6. Long term stability test of the oxidative reforming of methane on Ni20YZ.

to achieve the oxidative reforming of methane, the YZ supports (20YZ and 40YZ) converted a significant amount of the CH_4 supplied in the inlet stream (see the catalytic tests for pure supports 20YZ and 40YZ in Fig. 5a) and also produced a small net amount of CO_2 in the outlet stream (small negative values for CO_2 conversion on 20YZ and 40YZ, which are not shown in Fig. 5b) and traces of water were observed. These findings show that the POM reaction occurs by the combustion-reforming of methane pathway, by reactions (4)–(6).

Other studies affirm that oxygen vacancies dissociate CO_2 molecules [50], resulting in the release of CO and forming $\text{O}_{(\text{s})}$ species [46,47,51]. However, as was mentioned previously, the catalytic supports did not show any catalytic activity in the dry reforming of methane in the absence of oxygen. Moreover, according to the catalytic tests of the dry reforming of model biogas over the catalysts containing the three oxides, the oxygen vacancies were not very beneficial to this reaction, as samples Ni20YZ and Ni40YZ (which contain the highest concentrations of $\text{Y}_2\text{O}_3-\text{ZrO}_2$ solid solution) did not give the best performance; however, the oxygen vacancies were highly beneficial in the presence of oxygen.

The oxidative reforming of biogas over all catalysts showed a significant fall in the CO_2 conversion (see Fig. 5b), compared to the values found in dry reforming of biogas (see Fig. 4b), and that fall may result from the total combustion of methane in the POM pathway ($\text{CH}_4 + 2\text{O}_2 \rightarrow \text{CO}_2 + 2\text{H}_2\text{O}$), all reactions ((1) and (3)–(6)) occurring in parallel.

Moreover, the oxidative reforming of biogas recorded better values for the H_2/CO ratio (≈ 1 for Ni20YZ and Ni40YZ, see Fig. 5c) than did dry reforming ($\ll 1$, see Fig. 4c), indicating that the addition of oxygen to the dry reforming of biogas enhances hydrogen production, leading to H_2/CO ratios very close to stoichiometric.

Another factor that may be involved in the performance of the catalysts in the oxidative reforming of biogas is the concentration of nickel on the surface. The catalysts that gave high conversion values (Ni20YZ and Ni40YZ) possessed a relatively high nickel concentration (see Table 1) and low dispersion of nickel on the surface (see Table 3). Therefore, they may have formed more active sites for all the reactions involved (reactions (1) and (3)–(6)); it seems that these active sites are allowed in the presence of oxygen, which may explain the good performance of Ni20YZ and Ni40YZ in the catalysis.

Conversely, the low performance of the catalysts NiY, NiZ and Ni4YZ in the oxidative reform of biogas (the lowest conversion values recorded), could be explained by a lack of active centers of Ni° on the surface of the catalysts for all the reactions involved in this process (reactions (1) and (3)–(6)). The analysis of the surface of



Fig. 7. SEM image (4000 \times) of Ni20YZ.

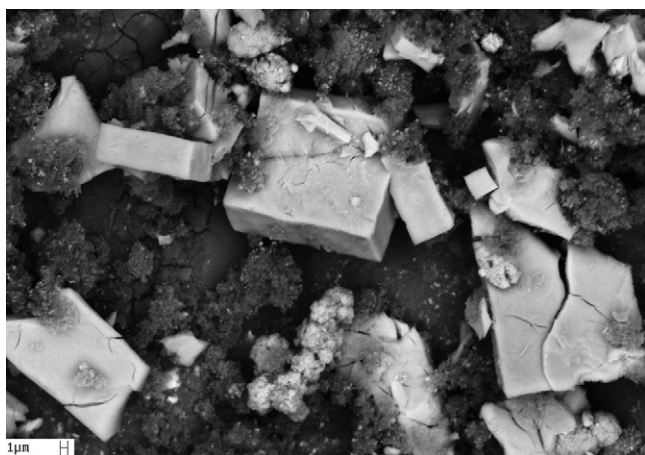


Fig. 8. SEM image (4000 \times) of Ni40YZ.

these three catalysts by XPS (Table 1) shows that they possess less nickel on the surface and the estimated dispersion of metallic nickel (Table 3) shows that these three catalysts have the highest dispersion, which may be related to their low performance, as the low atomic concentration of nickel on the surface may form fewer active sites for all reactions involved (reactions (1) and (3)–(6)).

Since the two best catalysts of our report (Ni20YZ and Ni40YZ) possess both NiO–Y₂O₃ and Y₂O₃–ZrO₂ solid solutions, the

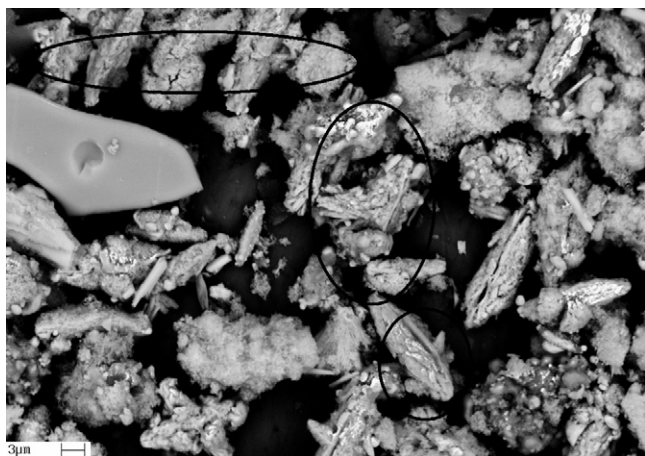


Fig. 9. SEM image (4000 \times) of Ni4YZ.

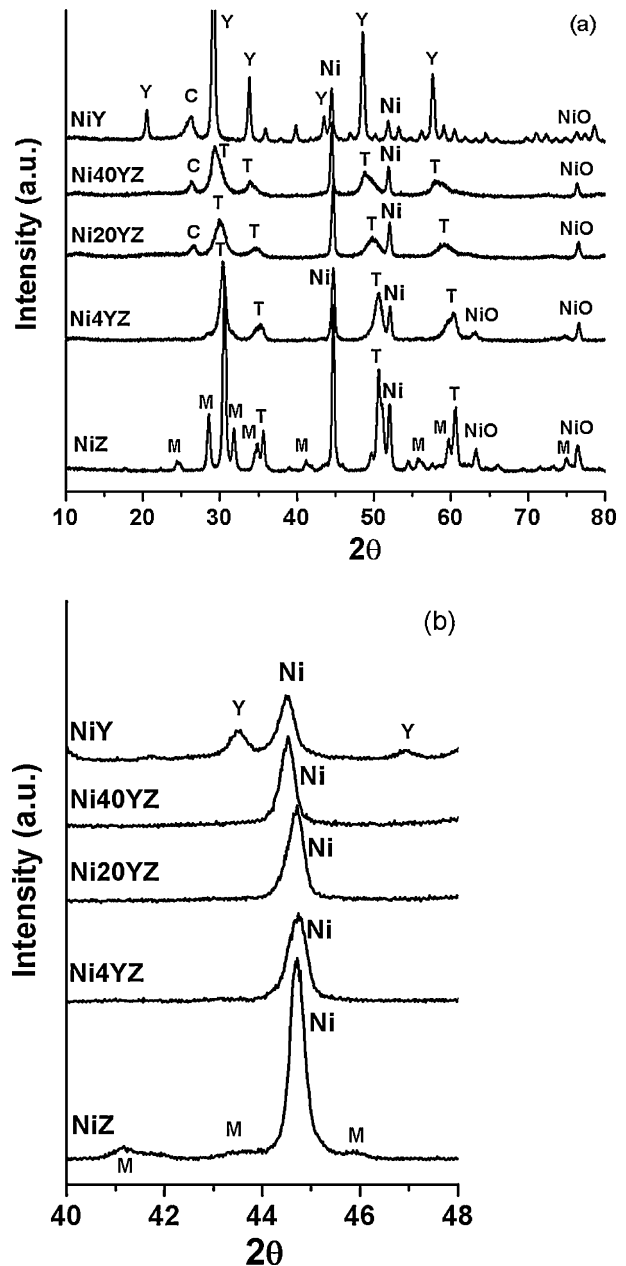


Fig. 10. XRD analysis of spent catalysts after 6 h of the oxidative reforming of biogas (a). Enlargement of pattern collected between angles 40° and 48° of the spent catalysts.

existence of a synergistic effect between these solid solutions during the oxidative reforming of biogas is suggested. This is supported by the fact that the solid solution NiO–Y₂O₃ (NiY sample) was deactivated during the reaction, while the Y₂O₃–ZrO₂ solid solution (40YZ and 20YZ supports) showed low catalytic activity (see Fig. 5a and b); thus, high conversion rates occurred when these two solid solutions were present in large amounts in the composition of the catalysts (Ni20YZ and Ni40YZ).

The rates of coke deposition on the catalysts during the dry reforming and oxidative reforming of biogas are shown in Table 4. It can be seen that coke deposition was greater during dry reforming and decreased in the presence of oxygen. Ni20YZ performed best in the oxidative reforming of biogas, because it achieved a relatively high rate of conversion (see Fig. 5a) and a relatively low coke deposition.

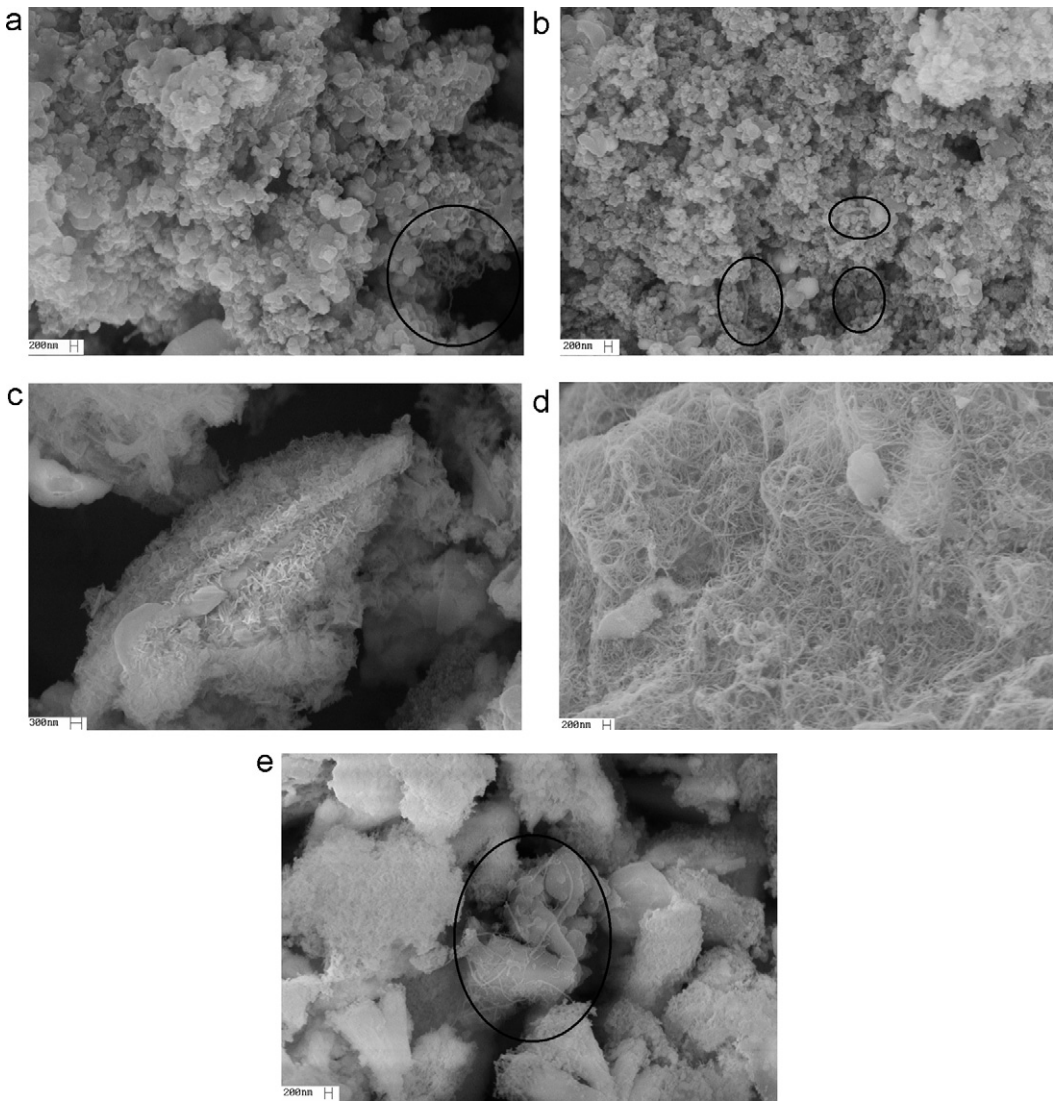


Fig. 11. SEM images (25,000 \times) of spent catalysts: (a) Ni40YZ; (b) Ni20YZ; (c) Ni4YZ; (d) NiY; and (e) NiZ.

The removal of carbon deposits may be assisted by the addition of oxygen, as well as by the oxygen vacancies formed by the Y_2O_3 – ZrO_2 solid solution, which increase the number of $\text{O}_{(s)}$ species. This is due to the reaction of the surface $\text{O}_{(s)}$ species (produced by dissociation of O_2) with the surface carbon species ($\text{CH}_x + \text{O}_{(s)} \rightarrow \text{CO} + x\text{H}; x = 1, 2, 3$).

Overall values of the H_2/CO ratio in the products (Fig. 5c) are lower than 1.2, which is the stoichiometric value for the oxidative reforming of biogas, because of the RWGSR ($\text{CO}_2 + \text{H}_2 \leftrightarrow \text{CO} + \text{H}_2\text{O}$) occurring during the reaction. The lower values of the H_2/CO ratio for the NiZ, NiY and Ni4YZ samples indicate the greater rate of the RWGSR on these catalysts.

The low performance of catalysts NiZ and NiY may be caused by the preparation method, since it has been shown elsewhere that the performance of these catalysts is strongly influenced by the method of preparation of the catalysts [52]. Thus, the present result suggests that the single-step polymerization method leads to good results only for the mixtures of three oxides, NiO , Y_2O_3 and ZrO_2 (the best performance being exhibited by Ni20YZ and Ni40YZ).

The conversion profiles of CH_4 and CO_2 in the catalysis of the oxidative reforming of biogas by the sample NiAlcom are shown in Fig. 5a and b. These results show that initially this catalyst has a high activity. However, the reaction was carried out for only

3.5 h, owing to the large amount of coke deposited (1.42 mmol h^{-1}), which caused the pressure in the reactor to rise rapidly. In this context, the Ni20YZ and Ni40YZ catalysts reported here are better than the commercial sample, and therefore promising materials for the oxidative reforming of biogas.

A long-term stability test was carried out on the best catalyst in the present study (Ni20YZ), which was tested under reaction conditions for 24 h. The results are shown in Fig. 6, where it can be seen that the catalyst maintained its activity for 24 h. A gradual continuous decrease in the reactant conversion rates was observed during the reaction, but this seemed to stabilize after 19 h of reaction, as after this time the conversion value remained constant at 63%. The H_2/CO ratio (≈ 1) was almost constant throughout the reaction. As was mentioned earlier, this value is a little lower than the stoichiometric values since the RWGSR occurs in parallel (traces of water were collected after the catalytic test). The rate of coke deposition over 24 h was 0.17 mmol h^{-1} on Ni20YZ, this value being close to that found for the catalytic test over 6 h of reaction.

A morphological analysis of catalysts after 6 h of the oxidative reforming of biogas was carried out by SEM and the results are shown in Figs. 7–9. Figs. 7 and 8 show SEM images of regions rich in zirconium and yttrium (determined by EDX analyses). The mixture of Y_2O_3 and ZrO_2 formed symmetric solid particles of

rectangular parallelepiped form. The sample of Ni20YZ consisted of larger particles.

The SEM image of a region of Ni4YZ (Fig. 9) rich in nickel, zirconium and yttrium shows that, on this sample, zirconia particles formed a block of undefined form (on the left side in Fig. 9), while nickel formed aggregates shaped like capsules (marked with black lines in Fig. 9). This morphology is very different from that found in Ni20YZ and Ni40YZ. The aggregated particles of nickel found on Ni4YZ suggest a sintering of nickel in this region, which may be related to the low activity of this catalyst in the oxidative reform of biogas. SEM images of NiZ and NiY catalysts (not shown) did not show particles of any defined form in regions rich in zirconium and yttrium. The XRD patterns of spent catalysts after 6 h of the oxidative reform of biogas (Fig. 10a) show that catalysts without yttrium or with low yttrium content (NiZ, Ni4YZ) form an amorphous carbon whose structure is undetectable by XRD. In this figure, it is clearly seen that the presence of further yttrium favored the formation of graphitic carbon (on Ni40YZ and Ni20YZ), and NiY shows the strongest peak for graphitic carbon. Fig. 10b shows an enlargement of the pattern between Bragg angles 40° and 48°, which contains the principal peak of Ni^o; the Ni^o crystallite sizes were 31, 22, 26, 29 and 23, for NiZ, Ni4YZ, Ni20YZ, Ni40YZ and NiY; this trend is the same as that found for the crystallites of Ni^o on the fresh catalysts after reduction (Table 3). In reforming methane reactions there are two principal forms of carbon deposit: encapsulating and filamentous [53]. The filamentous carbon is formed by dissolution of the carbon in nickel and its subsequent precipitation at the rear of the metal particle, which forces this particle off the catalytic support surface to form the filaments. Both types of carbon, encapsulated and filamentous, are actively gasified in reforming methane reactions, but the rate of gasification depends on their amount, reactivity and location on the surface of the catalyst [54].

Fig. 11a–e shows SEM images of used catalysts after 6 h of oxidative reform of biogas, in a region rich in carbon (according to EDX analysis). In these pictures, the morphology of the coke formed on NiZ, NiY and Ni4YZ is that of filamentous carbon, the filaments being longest on sample NiY. SEM images of coke on Ni20YZ (Fig. 11b) and Ni40YZ (Fig. 11a) are very similar to each other, with very little formation of filamentous carbon. Most of this coke has no defined morphology, suggesting the deposition of a graphitic carbon or amorphous morphology.

From the overall images of coke (Fig. 11a–d), it is possible to correlate the type of carbon deposit with the catalytic activity of the catalysts. Thus, the low conversion rates during the oxidative reform of biogas on the catalysts NiZ, Ni4YZ and NiY (Fig. 4) may be explained by the presence of filamentous carbon, since it is known that filamentous carbon can accumulate on the metallic particle, resulting in a loss of active centers. Furthermore, the presence of filamentous graphitic carbon on sample NiY (as seen by XRD in Fig. 10a) was most prejudicial, since this sample had the worst stability and a low conversion rate, implying that this carbon is hardly gasified during the reaction.

The carbon of amorphous morphology (Fig. 11a and b) on the surface of Ni20YZ and Ni40YZ (which is of graphitic structure, according to see Fig. 10), seems not to affect the activity of these catalysts, since they exhibited higher stability and higher conversion rates than NiZ, NiY and Ni4YZ. In this light, this carbon seems to be gasified easily during oxidative reforming and it is probably in close contact with the nickel particles and/or is situated in the vicinity of the oxygen vacancies (formed by Y₂O₃–ZrO₂), resulting in high gasification activity that leads to high conversion rates [55,56]. Similar results were found by Wang and Lu [54] and Khan et al. [57] in the CO₂ reforming of methane on Ni catalysts.

Finally, despite the fact that it is unclear whether or not oxygen vacancies inhibit the formation of filamentous carbon, the results shown in Fig. 1 and Fig. 11a–e suggest that the presence of greater

amounts of Y₂O₃–ZrO₂ solid solution seems to inhibit the formation of filamentous carbon (this form of carbon being harmful to the catalytic activity).

4. Conclusions

The following conclusions can be drawn from this research:

The results presented here demonstrate that the addition of Y₂O₃ to the Ni/ZrO₂ system, by the one-step chemical polymerization method, improved the performance of the catalysts in the oxidative reforming of biogas.

The Y₂O₃ added to the NiO/ZrO₂ system formed NiO–Y₂O₃ and Y₂O₃–ZrO₂ solid solutions. The presence of these solid solutions had positive effects on the performance of the catalysts in the oxidative reforming of biogas. The Y₂O₃–ZrO₂ solid solution has catalytic activity in POM reaction which favored the conversion of CH₄ during the oxidative reforming of biogas.

The generation of oxygen vacancies, due to the formation of Y₂O₃–ZrO₂ solid solution, promoted the removal of the coke deposited on the Ni^o surface, since Ni20YZ showed the highest conversion and a relatively low amount of coke during the oxidative reforming of biogas. The good performance of Ni20YZ is due to a good balance between the number of active sites of Ni^o and oxygen vacancies nearby. The presence of yttria (in the 3-oxide mixtures) favored the formation of amorphous graphitic carbon. The formation of filamentous carbon hindered the catalytic activity of catalysts with little or no Y₂O₃. The filamentous carbon of graphitic structure was the most prejudicial to catalytic performance, leading to poor stability and a low conversion rate.

Overall results suggest that the formation of Y₂O₃–ZrO₂ solid solution inhibits the formation of filamentous carbon, the form of carbon most prejudicial to the catalytic activity in the oxidative reforming of model biogas.

Acknowledgements

The authors thank the Brazilian National Council for Scientific Development (CNPq) for the fellowship, and the Brazilian Synchrotron Light Laboratory (LNLS) in Campinas, Brazil, for the *in situ* XRD analysis.

References

- [1] S.N. Naik, V.V. Goud, P.K. Rout, A.K. Dalai, Renewable and Sustainable Energy Reviews 14 (2010) 578–597.
- [2] J. Xu, W. Zhou, Z. Li, J. Wang, J. Ma, International Journal of Hydrogen Energy 34 (2009) 6646–6654.
- [3] A. Effendi, K. Hellgardt, Z.G. Zhang, T. Yoshida, Fuel 84 (2005) 869–874.
- [4] A.F. Lucrecio, J.M. Assaf, E.M. Assaf, Applied Catalysis A-General 400 (2011) 156–165.
- [5] N. Rueangjitt, C. Akarawitoo, S. Chavadej, Plasma Chemistry and Plasma Processing 32 (2012) 583–596.
- [6] A. García, A. Martínez, Applied Catalysis A-General 411–412 (2012) 170–179.
- [7] D. Mao, J. Xia, Q. Chen, G. Lu, Catalysis Communications 10 (2009) 620–624.
- [8] C.W. Forsberg, International Journal of Hydrogen Energy 32 (2007) 431–439.
- [9] Y.J.O. Asencios, J.D.A. Bellido, E.M. Assaf, Applied Catalysis A-General 397 (2011) 138–144.
- [10] M. Benito, S. García, P. Ferreira-Aparicio, L. García-Serrano, L. Daza, Journal of Power Sources 169 (2007) 177–183.
- [11] P. Kolbitsch, C. Pfeifer, H. Hofbauer, Fuel 87 (2008) 701–706.
- [12] A. Effendi, Z.G. Zhang, K. Hellgardt, K. Honda, T. Yoshida, Catalysis Today 77 (2002) 181–189.
- [13] S. Bharadwaj, L. Schmidt, Fuel Processing Technology 42 (1995) 109–127.
- [14] A. York, T. Xiao, M. Green, Topics in Catalysis 22 (2003) 345–358.
- [15] A. Raju, C. Park, J. Norbeck, Fuel Processing Technology 90 (2009) 330–336.
- [16] Y.J.O. Asencios, P.A.P. Nascente, E.M. Assaf, Fuel 97 (2012) 630–637.
- [17] P. Kumar, Y. Sun, R.O. Idem, Energy and Fuels 21 (2007) 3113–3123.
- [18] J.D.A. Bellido, E.M. Assaf, Applied Catalysis A-General 352 (2009) 179–187.
- [19] M.H. Youn, J.G. Seo, J.C. Jung, J.S. Chung, I.K. Song, Catalysis Surveys from Asia 14 (2010) 55–63.
- [20] J.D.A. Bellido, J.E. De Souza, J.M. Peko, E.M. Assaf, Applied Catalysis A-General 358 (2009) 215–223.

[21] D. Srinivas, C.V.V. Satyanarayana, H.S. Potdar, P. Ratnasamy, *Applied Catalysis A-General* 246 (2003) 323–334.

[22] X. Deng, J. Sun, S. Yu, J. Xi, W. Zhu, X. Qiu, *International Journal of Hydrogen Energy* 33 (2008) 1008–1013.

[23] J.A. Montoya, E. Romero-Pascual, C. Gimón, P. Del Angel, A. Monzón, *Catalysis Today* 63 (2000) 71–85.

[24] V.M. Souza, D.A.G. Aranda, M. Schmal, *Journal of Catalysis* 204 (2001) 498–511.

[25] J.M. Wei, B.Q. Xu, J.L. Li, Z.X. Cheng, Q.M. Zhu, *Applied Catalysis A-General* A196 (2000) 167–172.

[26] K. Hiroki, T. Sekino, T. Kusunose, T. Nakayama, Y. Yamamoto, K. Niihara, *Materials Letters* 57 (2003) 1624–1628.

[27] X. Yin, L. Hong, Z. Liu, *Journal of Physical Chemistry C* 111 (2007) 9194–9202.

[28] Y. Wang, X. Hong, B. Li, W. Wang, D. Wang, *Journal of Natural Gas Chemistry* 17 (2008) 344–350.

[29] S. Chien, W. Chiang, *Applied Catalysis A* 961 (1990) 45–61.

[30] C.H. Bartholomew, R.B. Pannell, *Journal of Catalysis* 65 (1980) 390–401.

[31] R.D. Jones, C.H. Bartholomew, *Applied Catalysis A-General* 39 (1988) 17–88.

[32] J. Zhang, H. Wang, A. Dalai, *Applied Catalysis A-General* 339 (2008) 121–129.

[33] J.H. Sepulveda, N.S. Figoli, *Applied Surface Science* 68 (1993) 257–264.

[34] G. Fagherazzi, A. Benedetti, S. Polizzi, *Catalysis Letters* 32 (1995) 293–303.

[35] A.L. Bonivardi, M.A. Baltanas, *Journal of Catalysis* 138 (1992) 500–517.

[36] D. Xu, W. Li, H. Duan, Q. Ge, H. Xu, *Catalysis Letters* 102 (2005) 229–235.

[37] S.T. Hussain, *Journal of the Chemical Society of Pakistan* 17 (1995) 125–128.

[38] A.M. Venezia, L.F. Liotta, G. Pantaleo, V. La Parola, G. Deganello, A. Beck, Z. Koppány, K. Frey, *Applied Catalysis A-General* 251 (2003) 359–368.

[39] F. Parmigiani, F.E. Depero, L. Sangaletti, G. Somaggia, *Journal of Electron Spectroscopy and Related Phenomena* 63 (1993) 1–10.

[40] S. Damynova, B. Pawelec, K. Arishtirova, M.V. Martinez-Huerta, J.L.G. Fierro, *Applied Catalysis A-General* 337 (2008) 86–96.

[41] V. Craciun, J. Howard, E.S. Lambers, R.K. Singh, D. Craciun, J. Perriere, *Applied Physics A* 69 (1999) 535–538.

[42] A. Parmaliana, F. Arena, F. Frusteri, S. Coluccia, L. Marchese, G. Martra, A.L. Chuvalin, *Journal of Catalysis* 141 (1993) 34.

[43] Y. Hu, E. Ruckenstein, *Advances in Catalysis* 48 (2004) 297–345.

[44] E. Ruckenstein, H.Y. Wang, *Catalysis Letters* 73 (2001) 99–105.

[45] X. Zhao, R. Geng, P. Tyagi, H. Hayano, S. Kato, M. Nishiwaki, T. Saeki, M. Sawabe, *Physical Review Special Topics – Accelerators and Beams* 13 (124702) (2010) 1–7.

[46] W. Dow, T. Huang, *Journal of Catalysis* 160 (1996) 155–170.

[47] L. Xiancai, L. Shuigen, Y. Yifeng, W. Min, H. Fei, *Catalysis Letters* 118 (2007) 59–63.

[48] H. Roh, K. Jun, S. Baek, S. Park, *Bulletin of the Korean Chemical Society* 23 (2002) 799–802.

[49] X. Xia, R.J. Oldman, C.R.A. Catlow, *Journal of Materials Chemistry* 22 (2012) 8594–8612.

[50] T. Huang, H. Lin, T. Yu, *Catalysis Letters* 105 (2005) 239–247.

[51] W. Dow, T. Huang, *Journal of Catalysis* 160 (1996) 171–182.

[52] S. Yue-Qin, H. De-Hua, X. Bo-Qing., *Applied Catalysis A-General* 337 (2008) 19–28.

[53] S. Wang, G.Q. Lu, *Industrial and Engineering Chemistry Research* 38 (1999) 2615–2625.

[54] S. Wang, G.Q. Lu, *Applied Catalysis A-General* 169 (1998) 271–280.

[55] D. Duprez, M. Hadj-Aissa, J. Barbier, *Applied Catalysis* 49 (1989) 67–74.

[56] D. Duprez, M. Hadj-Aissa, J. Barbier, *Studies in Surface Science and Catalysis* 68 (1991) 111–118.

[57] A. Khan, T. Sukonket, B. Saha, R. Idem, *Energy and Fuels* 26 (2012) 365–379.